

# Flow physics analysis of an auxiliary hole film cooling configuration : Part 2 - Large eddy simulations

Arunprasath Subramanian

Research scholar,  
Institut P'  
ISAE-ENSMA  
Poitiers, France 86000  
Email: arunprasath.subramanian@ensma.fr

Gildas Lalizel

Assistant professor  
Institut P'  
ISAE-ENSMA  
Poitiers, France 86000

Eva Dorignac

Professor  
Institut P'  
Department of Fluid, Thermal and Combustion(FTC)  
University of Poitiers  
Poitiers, France 86000  
Email: eva.dorignac@univ-poitiers.fr

Detailed descriptions of a novel film cooling configuration have been provided in this article through large eddy simulations. Novel anti-vortex hole shape called the auxiliary hole system is analysed in this study. The complex interactions between a jet emanating from a hole and another jet from a smaller hole placed behind is difficult to predict. Through this numerical analysis work which is compared with experiment results as well, important flow features in such a hole arrangement are identified. A comprehensive quantitative and qualitative analysis is provided for a blowing ratio of  $M=3$  and a crossflow temperature of  $150^{\circ}\text{C}$ . Instantaneous and mean temperature flow fields are presented for a simple cylindrical hole configuration and an auxiliary hole configuration to present the improvement in the flow features of the latter film cooling hole arrangement.

## Nomenclature

- A You may include nomenclature here.
- $\alpha$  There are two arguments for each entry of the nomenclature environment, the symbol and the definition.

## 1 Introduction

Film cooling techniques have been employed to improve the turbine inlet temperatures so as to improve the efficiency of a gas turbine engine. The multiple hole film cooling arrangement can be thought as a Jet in Cross Flow (JICF) type

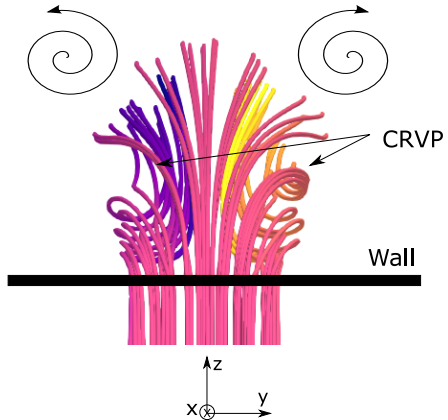


Fig. 1. View upstream of the hole showing the formation of the CRVP vortices in a jet emanating from an orifice: Single hole case at  $M=0.65$  (in-house study).

of problem. Typically, a cold jet is injected into the hot main-stream flow and the interaction of the jet with the cross flow yield interesting system of vortices. One of the major detrimental factors in the film cooling process is the presence of the Counter Rotating Vortex Pairs (CRVP). The formation of the CRVP is shown in the Fig. 1.

The CRVP is formed mainly due to the shear between the mainstream flow and the jet emanating out of the hole

which acts as a flexible obstacle to the flow ([1]). The reduction in the vortex intensity of the CRVP is found to improve the film cooling efficiency due to reduced interaction and mixing between the crossflow and the injected jet described by [2]. Consequently, efforts were made to understand the origins and structure of CRVPs by [3], [4], [5], [6], their structure and the ways to counter them by [7].

The blowing ratio ( $M$ ) which is the ratio of the coolant mass flux to the mainstream mass flux as defined by the expression 1 has a significant effect on the film cooling efficiency.

$$M = \frac{\rho_c U_c}{\rho_\infty U_\infty} \quad (1)$$

A low blowing ratio (less than 1) means that the coolant jet remains attached to the wall to be cooled. For a blowing ratio of 1, a jet lift-off can be seen which means that the coolant jet takes off from the surface initially. But the momentum of the mainstream flow pushes the jet back towards the wall and hence a reattachment is seen. At higher blowing ratios, the jet penetrates deep into the mainstream flow and never reattaches at the wall.

This work is a continuation of the experimental analysis using phosphor thermometry presented in Part I. Time-resolved numerical analysis like the work of [8] has been carried out on film cooling configurations in the past to show the effect of CRVP on the film cooling effectiveness. However, few time-resolved studies exist on auxiliary hole configuration at high blowing ratios.

## 2 Current work

The present work aims to thoroughly study the effects of an auxiliary hole placed behind a main hole for the purpose of film cooling in turbine blades and combustion chambers. The following are the objectives of this study.

1. To obtain 3-D instantaneous flow features through large-eddy simulations on an auxiliary hole configuration.
2. Comparison of the temperature fields obtained through experimental and numerical analyses which validate the results obtained numerically.
3. Compare the coherent structures in a simple hole configuration and auxiliary hole configuration to understand the differences and the mechanism of the counter rotating vortex structure in the auxiliary hole system.

### 2.1 Reference Experiment

Experimental work on the same film cooling configuration has been presented in Part I of this work. The experimental data is used in this article to compare and analyse the results with the numerical simulations. A view of the test section used in the experiments is shown in figure 2.

The film cooling configurations are identical in the experimental and numerical simulations. It must be noted that

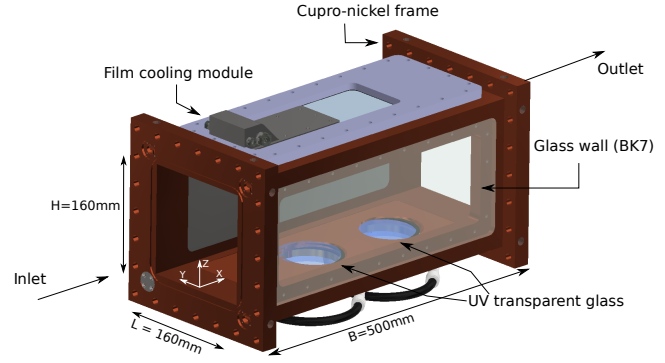


Fig. 2. Illustration of the modular test section with the various features.

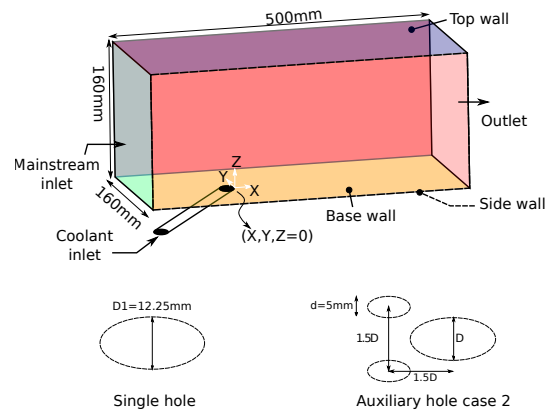


Fig. 3. Geometrical representation of the domain. The two geometric hole configurations are shown at the bottom.

a plenum is not added in the numerical simulations so as to be as close as possible to the experimental setup.

### 2.2 Computational setup

The geometry of the current problem is chosen to be as close as possible to the experimental film cooling case. The length of the domain is 500mm while the breadth and the height are fixed to be 160mm. Cold air is injected through a supply tube inclined at 30° towards the streamwise flow. The geometry is shown in the figure 3.

The turbulence length scale is fixed at 12.25mm due to the baseline single hole case diameter. An adiabatic wall condition is preferred as it is simple to analyse the adiabatic film cooling effectiveness. The boundary conditions are mentioned in the table 1.

### 2.3 Solver and Mesh sizing

All the numerical computations were carried out using StarCCM+ software (including geometry modeling, meshing, solving, and post-processing). Polyhedral mesh elements are used as they provide a balanced solution for complex mesh generation problems. They are relatively easy and efficient to build, requiring no more surface preparation than the equivalent tetrahedral mesh. They also contain approximately five times fewer cells than a tetrahedral mesh for a

Table 1. Boundary conditions used for the LES simulations

Parameter	Cross-flow	Jet
Mass flow	310g/s	4.45g/s and 1.44g/s
Temperature	150°C	20°C
Density	0.83kg/m <sup>3</sup>	1.32kg/m <sup>3</sup>
Turbulence intensity	7%	7%
Turbulence length scale	12.25mm	12.25mm
Blowing ratio 'M'		3
Density ratio		1.45

given starting surface.

In order to determine the right cell sizing to provide accurate results, the Taylor microscale was first computed using RANS simulations run on a coarse mesh with 1.5 million elements. The Taylor microscale is the intermediate length scale which lies at the dissipation region end of the inertial sub-range within the turbulence spectrum at which fluid viscosity significantly affects the dynamics of turbulent eddies in the flow. In other words, viscosity does not affect the length scales larger than the Taylor length scale strongly. Hence mesh elements of the order of this length scale is beneficial for the LES simulation to be acceptably accurate [9]. Upon determination of the zones where mesh refinements were required, two refinement zones were defined (zone 1 and zone 2 in figure 4). Maximum cell size in the zone 1 was fixed at 0.6mm and 1mm in zone 2. In all, the mesh contained 5.2 million elements for the single hole case and 5.8 million cells for the auxiliary hole case 2 configuration. At a blowing ratio of M=3, the wall Y+ remained less than 1 throughout the domain.

To initialise the LES simulations, a RANS simulation was run on the same LES mesh. k- $\omega$  SST turbulence model was used with the same boundary conditions as in the LES case. WALE subgrid scale model ([10]) is used to model the subgrid scale viscosity. The advantage of the WALE model is that it does not require any form of near-wall damping as it automatically gives accurate scaling at walls. Implicit unsteady scheme with second order temporal discretisation is used to improve accuracy. A convergence criteria called the Convective Courant Number is given as  $\frac{vdt}{dx}$  (where v is the velocity, dt is the time step, dx is the cell size). The time step was set at  $10^{-5}$ s for which the Convective Courant Number remained less than 1 throughout the domain, ensuring convergence. Figure 5 shows the Convective Courant Number in the central plane and the wall Y+ distribution on the base wall. In all, each simulation took about 5000 CPU hours for simulating 0.05s amounting to 3 complete flushes for the M=3 case.

### 3 Results

The discussion of the results obtained numerically and experimentally are presented in this section. This section

begins with a comparison of the results obtained by experiments, LES and RANS simulations for a blowing ratio of M=3.

#### 3.1 Mean temperature flow field

The mean non-dimensional temperature ( $\Theta$ ) flow field visualisation is presented in the figures 6-8 obtained by using phosphor thermometry, LES simulations and RANS simulations (which were used to initialize the LES simulations). LES simulations have a closer similarity to the experimental cases as compared to the RANS simulations. It should be noted that the experimental cases are an average of a limited number of acquisitions (100) as compared to the LES simulations with thousands of instances used for the averaging process. Despite this, there is a good qualitative accordance between these two visualisations.

$$\Theta = \frac{T_\infty - T}{T_\infty - T_c} \quad (2)$$

Figure 6 shows the non-dimensional temperature contour for Y=0 (central symmetry plane). Figures (a) and (b) are obtained through experiments using phosphor thermometry, figures (c) and (d) are obtained using LES simulations, while figures (e) and (f) are obtained from RANS simulations. Also, (a), (c) and (e) correspond to the single hole case while figures (b), (d) and (f) correspond to the auxiliary hole case 2 configuration.

From the presented figures, the trajectory of the jet and the effectiveness of the film close to the wall in the single and auxiliary hole cases can be visualised. The trajectory of the single hole case is much further away (1.5D away from the wall at X/D=4) from the wall as compared to the auxiliary hole case (0.7D away from the wall at X/D=4). The flow field in the region X/D<4 highlights the increased  $\Theta$  close to the wall for the auxiliary hole case.

Figure 7 shows the non-dimensional temperature contour in the XZ plane at Y/D=0.4 in the lateral direction.

Very interesting remarks can be made from the figure 7. The single hole case shows decreased  $\Theta$  values as compared to the case with Y/D=0. The mean  $\Theta$  distribution is comparable between the experimental (a) and LES results (c) for the single hole case but the RANS simulation case (e) tends to over-estimate  $\Theta$  values. On the other hand, all the three auxiliary hole cases (b, d, f) show very similar qualitative properties. The most prominent feature of all is the appearance of a cold streak emanating from the auxiliary hole, which is present just above the cold streak of the main hole jet. This can qualitatively confirm the validity of the LES simulations due to conformity with the RANS and experimental results. The RANS simulation predict that the combined jets from the auxiliary holes and the main hole penetrate deeper into the flow as compared to the LES or experimental cases.

Figure 8 shows the non-dimensional temperature contour in the XZ plane at Y/D=0.8 in the lateral direction.

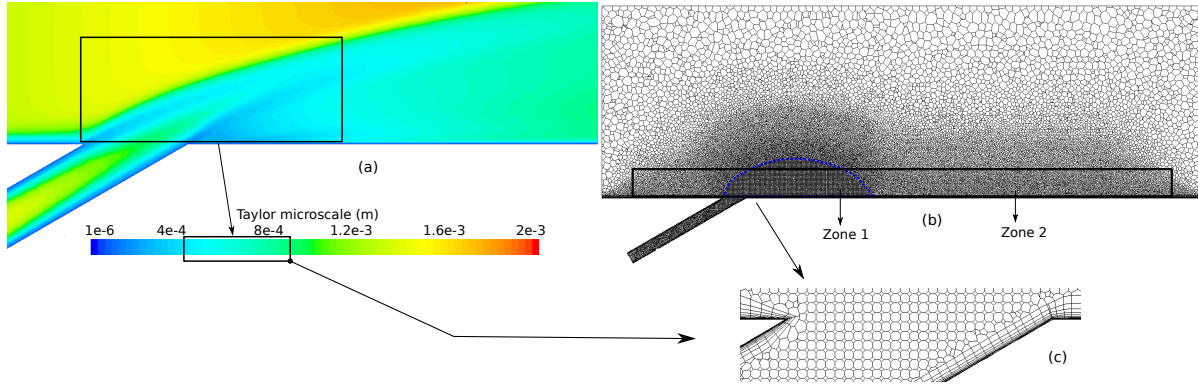


Fig. 4. (a) Determination of Taylor length scale from RANS simulation. (b) View of the mesh with 2 refinement zones. (c) Close-up view of the coolant exit region showing prism layers

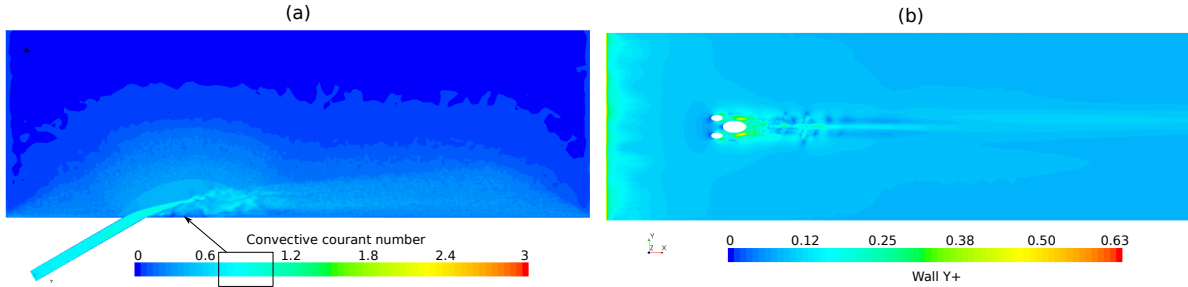


Fig. 5. (a) Convective Courant number distribution (b) Wall  $Y+$  distribution on the base wall.

The region at the hole exit of the single hole case has no presence of the injected cold jet. The presence of the jet flow is prominent in the region  $2 < X/D < 4$  where the expanding jet appears in the region away from the central axis of the jet. The LES case shows higher cold jet presence in the plane at  $Y/D=0.8$  than that of the RANS case. A study by [11] has shown that the RANS turbulence modelling tends to have an adiabatic film cooling effectiveness over-prediction in the regions closer to the central axis of the jet while the models under-predict the adiabatic film cooling effectiveness in the lateral directions as compared to experimental values. This shows that the RANS models tend to gather the jet flow closer to the central axis of the hole. The auxiliary hole case presents a different story compared to the single hole case. There is a much higher cold jet presence in the hole exit region compared to the single hole case, thanks to the presence of the laterally displaced auxiliary holes. Again, the flow tends to the closer towards the wall deeming higher adiabatic film effectiveness on the wall.

### 3.2 Adiabatic film cooling effectiveness

Looking at figure 9 (a) and (b) which presents the centerline and lateral adiabatic film cooling effectiveness respectively, it is clear that the auxiliary hole arrangement outperforms the single hole case at high blowing ratio ( $M=3$ ). This trend is seen throughout the longitudinal direction downstream of the hole exit. Due to the high momentum of the issuing jet, there is a dip in the centerline and laterally averaged adiabatic film cooling effectiveness at locations

$X/D < 5$ . However, due to intense mixing with the crossflow and partial reattachment, there is an improvement in the  $\eta$  values at locations  $X/D > 5$ .

Additionally, figure 10 shows the adiabatic film cooling effectiveness contour for the single hole and the auxiliary hole cases. The protection around the hole downstream of the hole is seen to have favourable lateral and longitudinal spread in the auxiliary hole case as compared to the single hole case.

With this, one can conclude some key aspects from all the obtained temperature field results so far.

Single hole case presents a higher jet penetration into the main flow as compared to the auxiliary hole case. Hence, on the first look, the auxiliary hole case tends to have better film cooling features.

RANS simulations over-predict the cold jet presence in the regions along the longitudinal axis of the jet and under-predict in the lateral zones.

In this section, it was seen that the auxiliary hole configuration performs better than the single hole system in terms of the non-dimensional temperature flow visualisations through experiments and numerical analyses. However, the better flow features of the auxiliary hole system is the consequence of a reason. There is a need to identify the cause of this effect and hence in the next section, a qualitative and quantitative analysis of the velocity, vorticity and temperature fields are discussed to understand the auxiliary hole configuration better.

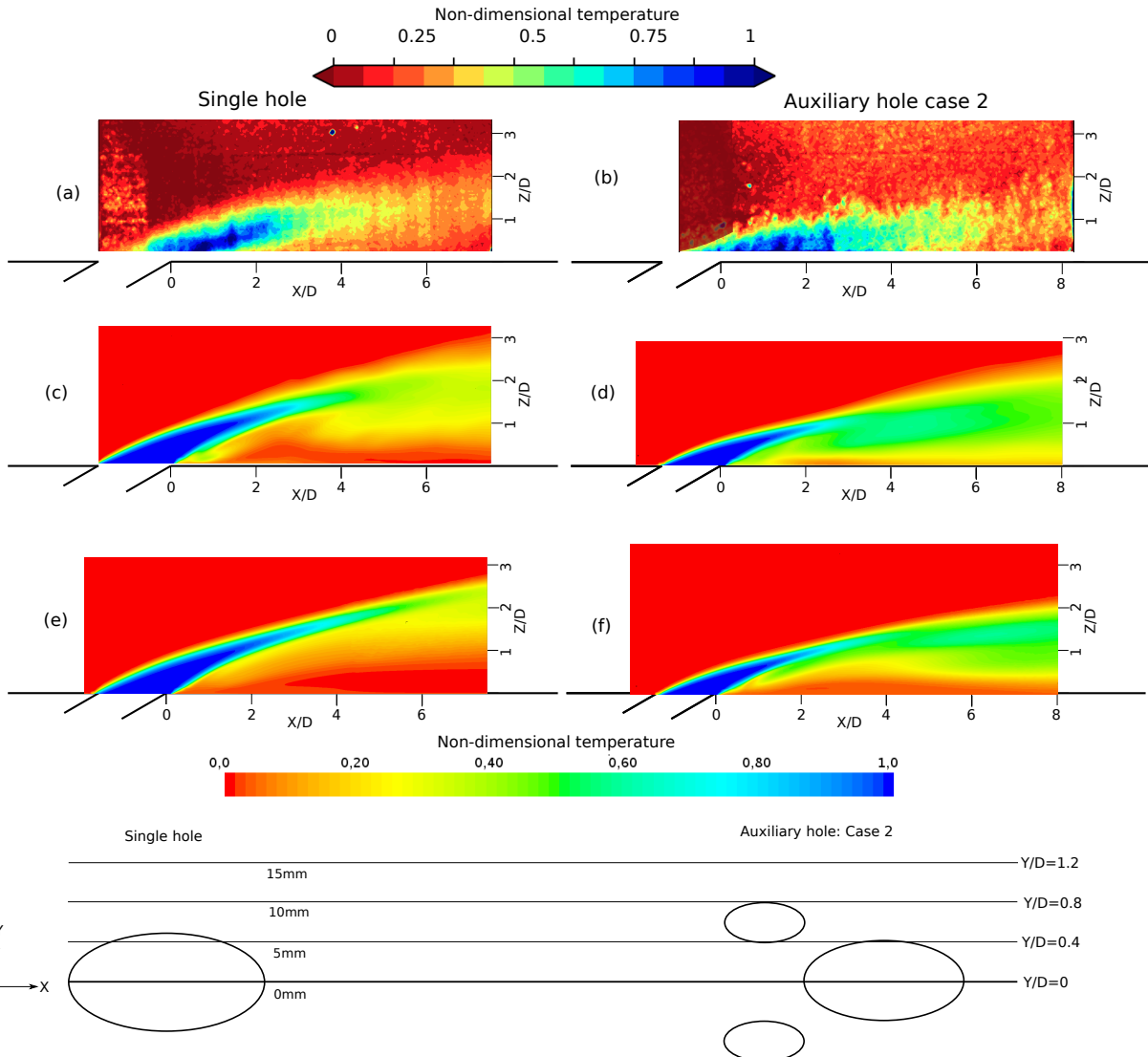


Fig. 6. Mean non-dimensional 2-D temperature contours in the XZ plane at  $Y/D=0$  for the single hole configuration (a, c, e) and the auxiliary hole configuration (b, d, f). The figures (a) and (b) are obtained using phosphor thermometry, (c) and (d) are obtained through LES simulations, (e) and (f) are obtained using RANS simulations.

#### 4 Discussion of flow physics

In this section, the physical phenomena occurring in the auxiliary hole configuration and the single hole configuration are discussed. RANS simulations cannot present instantaneous flow visualisations. However, LES simulations provide instantaneous flow data and can provide intricate details regarding coherent flow structures.

##### 4.1 Instantaneous temperature flow field

The instantaneous non-dimensional temperature ( $\Theta$ ) flow field visualisation is presented in the figures 11-13. Figures (a) and (b) are obtained through experiments using phosphor thermometry and figures (c) and (d) are obtained using LES simulations. Also, (a) and (c) correspond to the single hole case while figures (b) and (d) correspond to the auxiliary hole case 2 configuration. Figure 11 shows the non-dimensional temperature contour for  $Y=0$  (central symmetry

plane).

Comparing the single hole case and auxiliary hole case, one can observe that the jet in the single hole case tends to penetrate into the crossflow deeper than the auxiliary hole configuration which stays closer to the wall. Additionally, the jet-shear vortices in the windward and leeward side of the jet found in the experimental case are comparable to the numerical results. As previously mentioned, a  $\Theta$  value of 1 means purely cold injected jet, 0 represents purely hot crossflow, 0.5 refers to zones with perfect mixing between the crossflow and injected jet. The initial roll up of the top side jet shear layer induces strong mixing at a distance of 2-4 diameters away from the hole exit (values of  $\Theta$  around 0.5). The standing vortices are also clearly seen as marked with arrows. The zone under the ejecting jet is found to have  $\Theta$  values less than 0.3 indicating the predominant presence of crossflow closer to the wall. In the auxiliary hole case, the

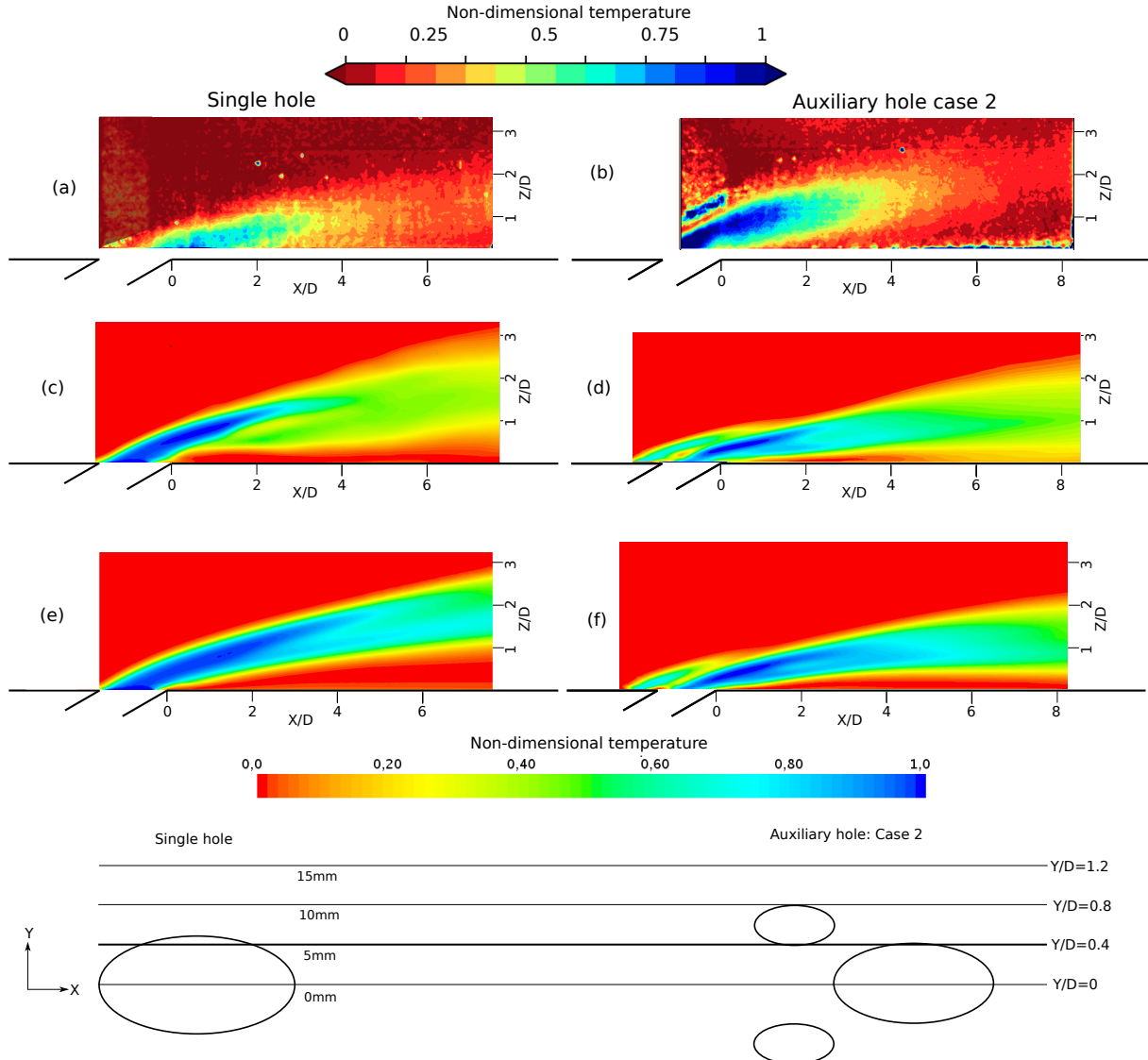


Fig. 7. Mean non-dimensional 2-D temperature contours in the XZ plane at  $Y/D=0.4$  for the single hole configuration (a, c, e) and the auxiliary hole configuration (b, d, f). The figures (a) and (b) are obtained using phosphor thermometry, (c) and (d) are obtained through LES simulations, (e) and (f) are obtained using RANS simulations.

Kelvin-Helmholtz roll up is not present, consequently periodic coherent structures are absent. The mixing between the main flow and the jet happens further downstream at about 4–6 diameters away from the hole exit. However, the extended zone with  $\Theta$  values around 0.6 indicate an addition of cold jet into the plane due to the auxiliary hole jet. It is also to be noted that  $\Theta$  values less than 0.2 in the zone close to the wall at  $1.5 > X/D < 2.5$  indicate side-wise ingestion of cross-flow due to horse-shoe vortices.

Figure 12 shows the non-dimensional temperature contour in the XZ plane at  $Y/D=0.4$  in the lateral direction.

Figure (a) presents similar flow features as seen in the case  $Y/D=0$ . However, the zone close to the wall has  $\Theta$  values around 0 indicating that the crossflow has been absorbed into the flow. This is the region below the CRVP structure and hence has high absorption of the crossflow under the jet. In the case of auxiliary hole, the auxiliary hole configuration

presents a jet flow closer to the wall and in addition to this, the  $\Theta$  values remain higher in the jet trajectory than that of the single hole. An interesting feature that can be observed in figures (b) and (d) is the presence of the auxiliary hole jet markedly seen just above the main hole jet. The zone marked 1 and 2 highlight this feature.

Figure 13 shows the non-dimensional temperature contour in the XZ plane at  $Y/D=0.8$  in the lateral direction.

Comparisons of figures (a) and (c) show good similarities between the LES and experimental results. Close to the jet exit, the jet is non-existent as the lateral spread is not quick enough to cover this zone. Further downstream, due to the expansion of the jet in the lateral directions, the jet flow appears as discontinuous streaks (due to Kelvin-Helmholtz instabilities). The auxiliary hole configuration presents a different scenario. Due to the presence of supporting auxiliary holes, the protection in the lateral direction is higher than

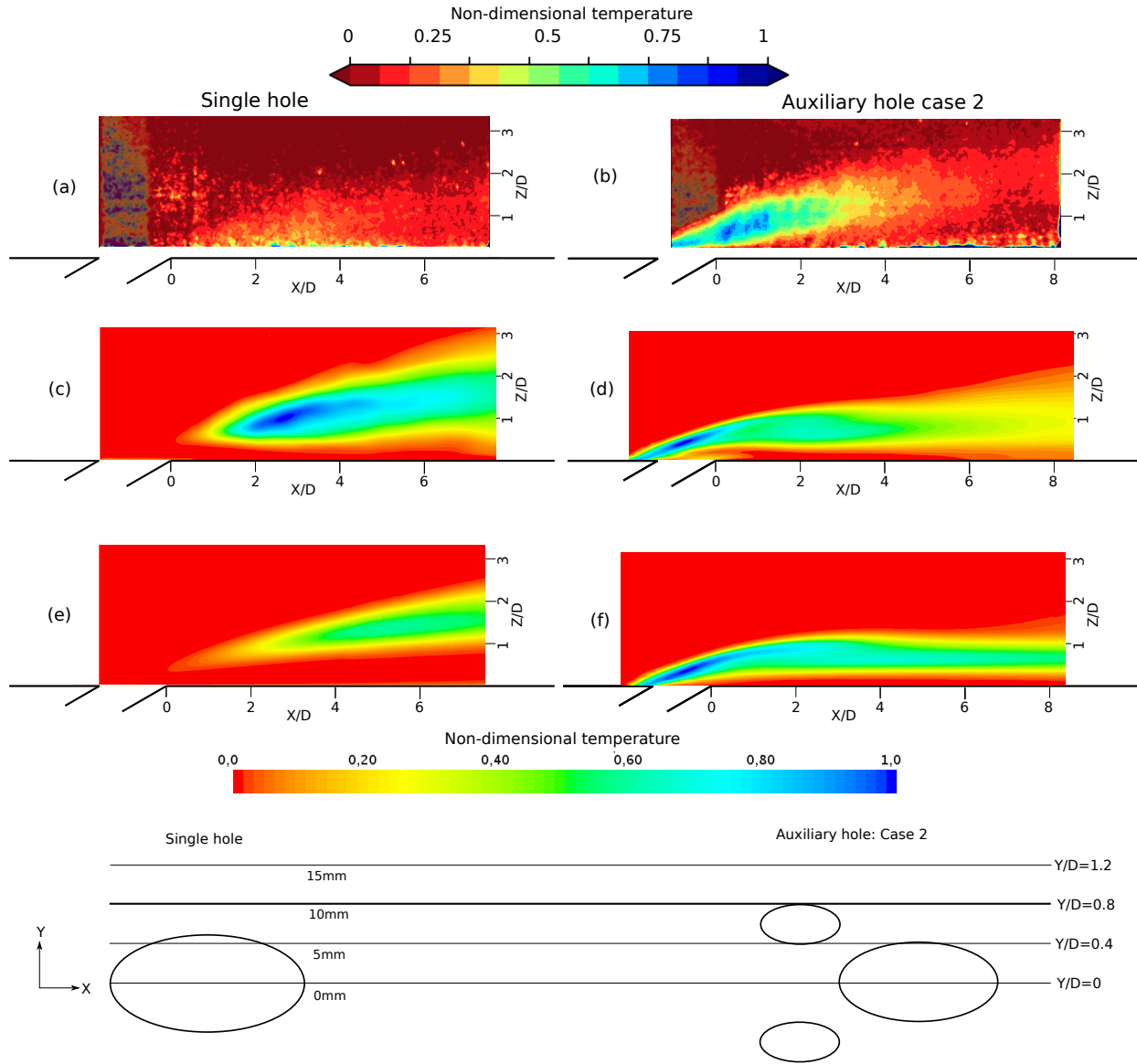


Fig. 8. Mean non-dimensional 2-D temperature contours in the XZ plane at  $Y/D=0.8$  for the single hole configuration (a, c, e) and the auxiliary hole configuration (b, d, f). The figures (a) and (b) are obtained using phosphor thermometry, (c) and (d) are obtained through LES simulations, (e) and (f) are obtained using RANS simulations.

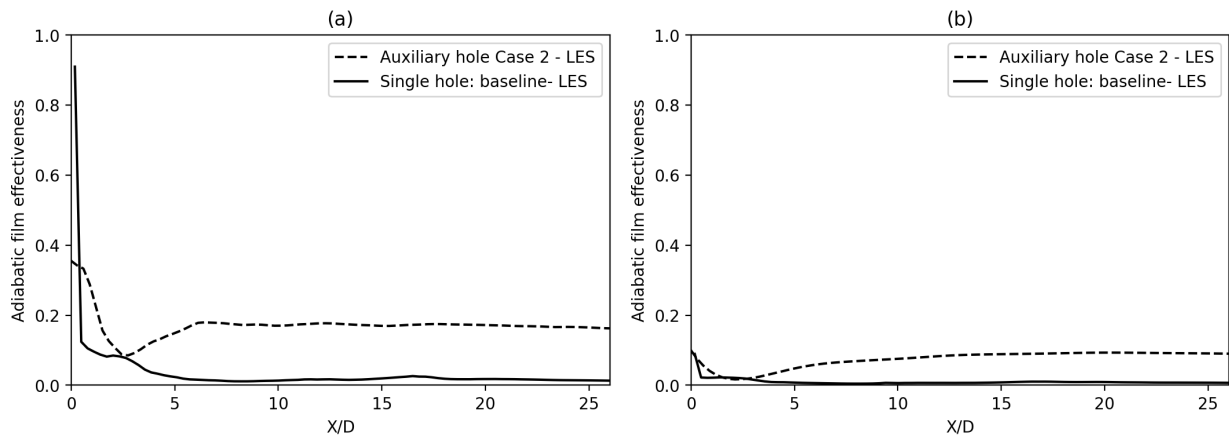


Fig. 9. Adiabatic film cooling effectiveness evolution for  $M=3$ .

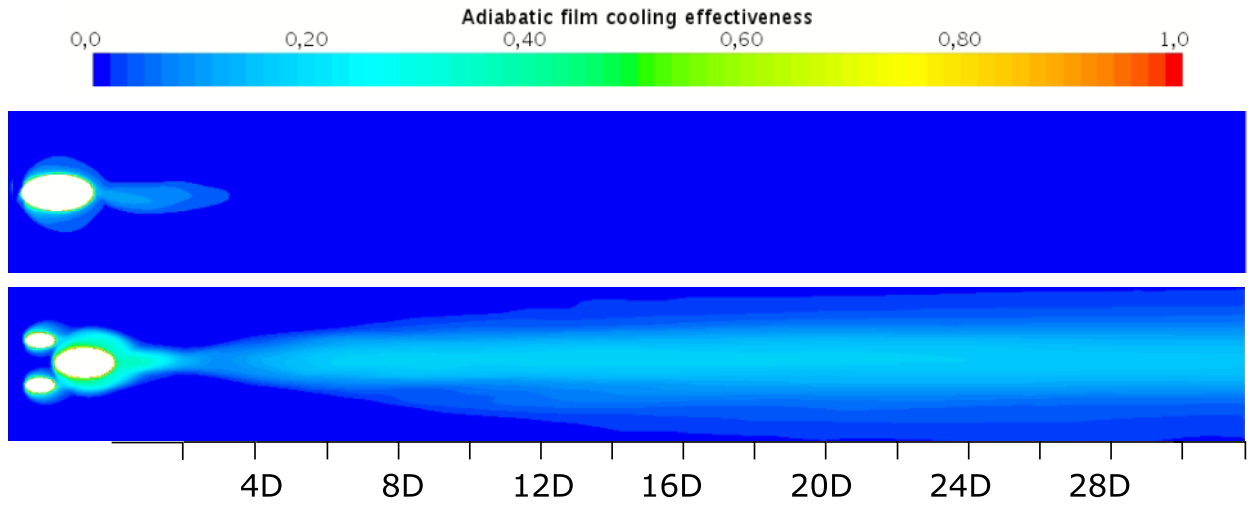


Fig. 10. Adiabatic film cooling effectiveness contours for  $M=3$ . Top: Single hole, bottom: Auxiliary hole case 2

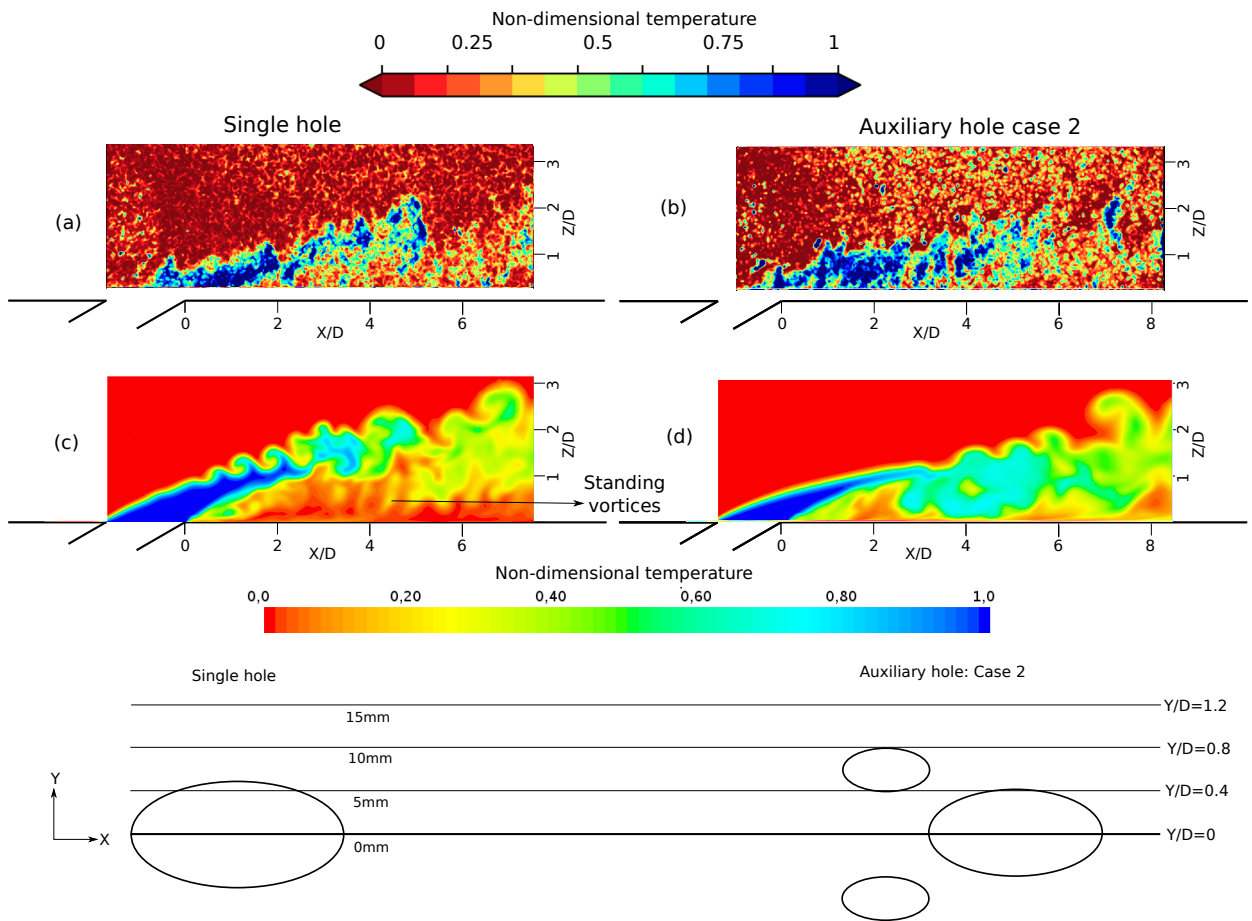


Fig. 11. Instantaneous non-dimensional 2-D temperature contours in the XZ plane at  $Y/D=0$  for the single hole configuration (a and c) and the auxiliary hole configuration (b and d). The figures (a) and (b) are experimentally obtained using phosphor thermometry and (c) and (d) are obtained through LES simulations.

that of the single hole case. As in previous cases, there is a good accordance in the qualitative features between the experimental and LES simulations as can be seen in (b) and (d).

Experimental and LES simulations have great accordance

with each other qualitatively and hence validate each other. Instantaneous flow fields have shown that the 2-D phosphor thermometry is accurate as it captures the instabilities like the jet-shear layer vortices and also the presence of the cold jet in intricate and difficult to identify zones.

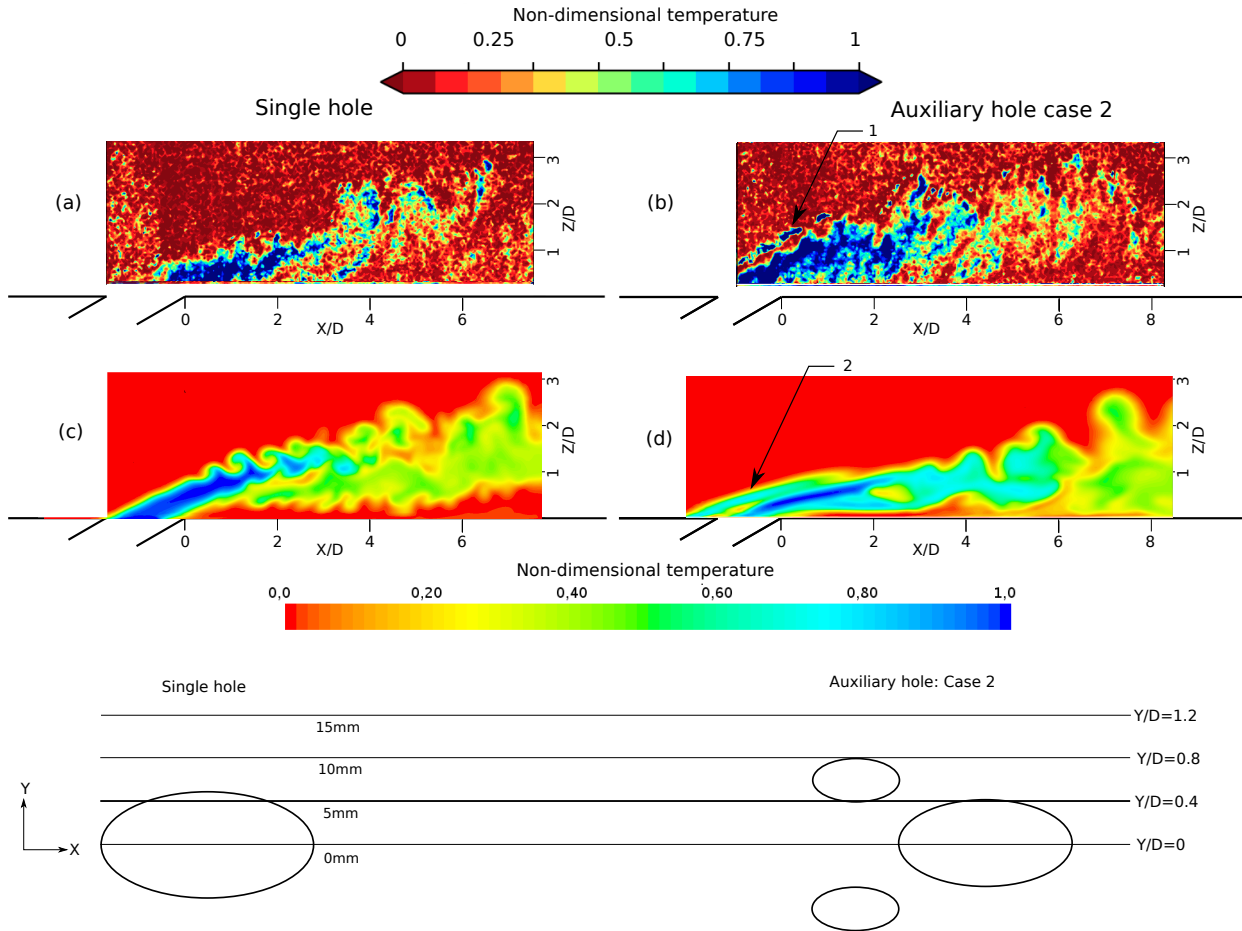


Fig. 12. Instantaneous non-dimensional 2-D temperature contours in the XZ plane at  $Y/D=0.4$  for the single hole configuration (a and c) and the auxiliary hole configuration (b and d). The figures (a) and (b) are obtained using phosphor thermometry and (c) and (d) are obtained through LES simulations.

## 4.2 Velocity and vortex field

The mean velocity contour for the single hole and auxiliary hole configuration is presented in the figure 14. The central XZ plane ( $Y=0$ ) is shown in this figure. As discussed previously, the jet from the single hole configuration penetrates deeper ( $Z/D=2$  at  $X/D=6$ ) into the flow compared to the flow from the main hole of the auxiliary hole configuration ( $Z/D=1$  at  $X/D=6$ ). Not only is the jet trajectory closer to the wall, but also the higher velocity downstream shows higher cold injected jet presence. This is not very explanatory to understand the mixing zones. Hence in figure 15, the variance of temperature, velocity (magnitude) and the  $i$ ,  $j$ ,  $k$  components of the velocity are presented. The variances are normalised as follows Temperature :  $T_{norm} = \frac{T_\infty - T_c}{T_\infty - \sqrt{Variance}}$

$$\text{Velocity : } V_{norm} = \frac{\sqrt{Variance}}{V_{max}}$$

Figures (a, c, e, g, i) present the variance contours for the single hole case and (b, d, f, h, j) present variance contours for the auxiliary hole configuration. The presentation of the variance in velocity and temperature is useful to determine the zones where there are strong fluctuations in temperature and zones with high mixing between the cold jet and the hot main flow. From the figures (a, c) and (b, d) one can understand that there is a strong correlation between the fluctua-

tions in temperature and velocity. The zones where there is a variation in the velocity (magnitude and  $i$ ,  $j$ ,  $k$  components) are an indicator of the wake region behind the jet. The comparison of (c) and (d) shows that fluctuations in velocity for the single hole case is along the jet-shear layer of the injected jet while for the auxiliary hole case, there are fluctuations in the near wall region downstream of the hole exit in addition to the jet shear layer vortices. A similar trend is also seen in (a) and (b) showing the variation of temperature. Looking at the individual components of velocity, (e, f) show the variance in the  $i$  component of the velocity. This field is very similar to the variance in velocity magnitude. However (g) and (h) representing the variation in the  $j$  component of the velocity are very different for the single hole and the auxiliary hole configurations. Along the central plane, there is very less lateral variation of velocity for the single hole case. In contrast, for the auxiliary hole case, there is a strong variation in the  $j$  component at the exit of the hole, and this can be attributed to a strong negative pressure gradient which attracts the jet from the auxiliary hole into the axis of the main hole. The periodic oscillation of sucking in the left and right auxiliary hole jet into the mainstream is the cause of this high variance at the jet exit. The  $k$  component of the velocity

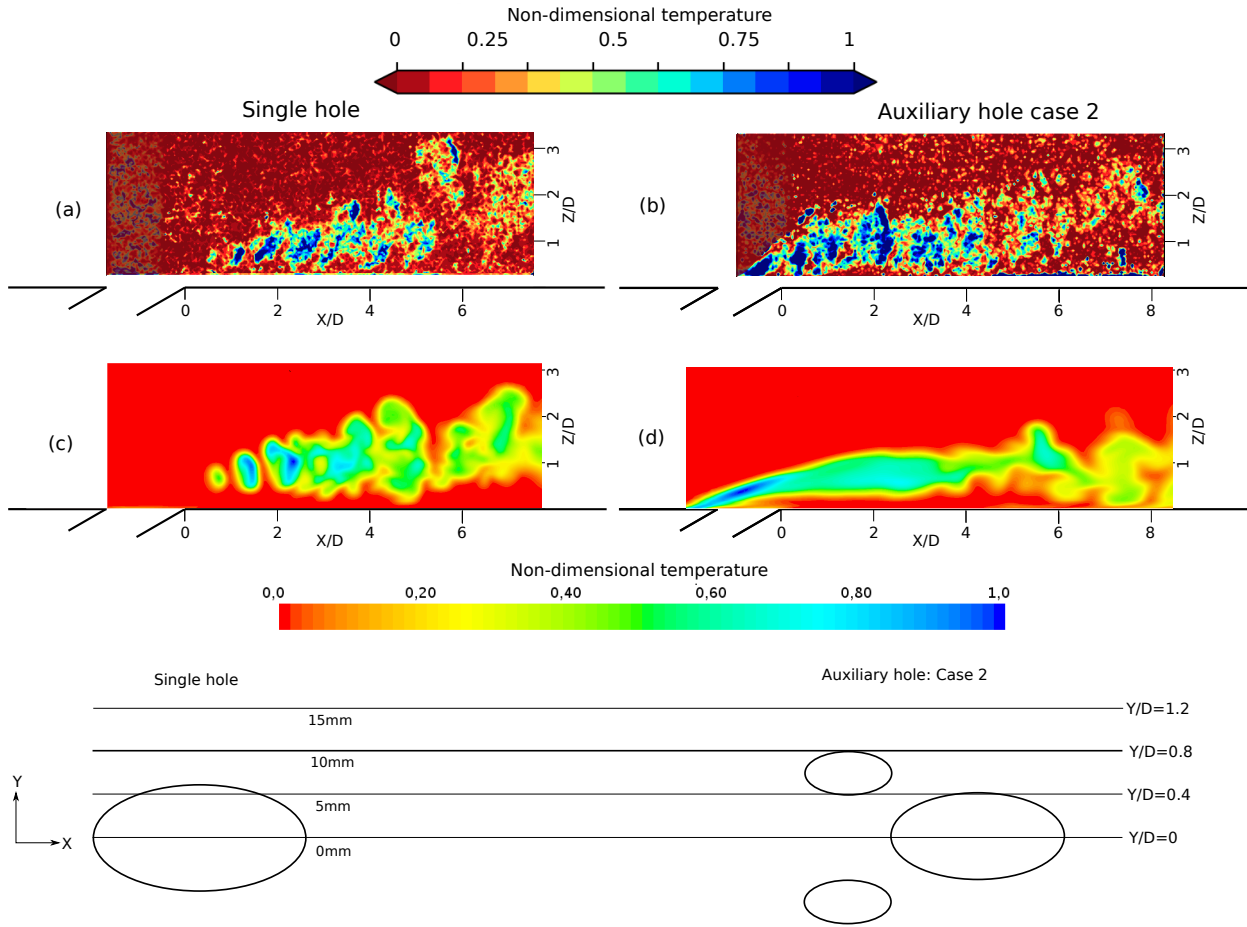


Fig. 13. Instantaneous non-dimensional 2-D temperature contours in the XZ plane at  $Y/D=0.8$  for the single hole configuration (a and c) and the auxiliary hole configuration (b and d). The figures (a) and (b) are obtained using phosphor thermometry and (c) and (d) are obtained through LES simulations.

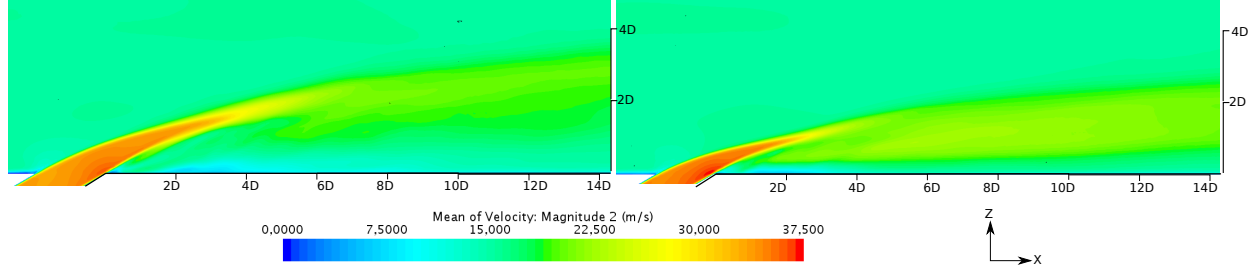


Fig. 14. Mean velocity contour in the central plane ( $Y/D=0$ ) for the single hole case (left) and the auxiliary hole configuration (right).

shows similar variance for the two hole configurations. Due to the enhanced mixing between the jet and the main hole caused by the Kelvin-Helmholtz instabilities, the maximum variation happens at the edges of the ejected jet (windward and leeward side). The combination of the variation of the three velocity components represent the overall wake region and the eventual mixing zones in the central plane.

Figure 16 shows the evolution of the mean helicity through the presentation of the front view (upstream of the hole). Helicity is defined as the product of the velocity and vorticity which is not only an indicator of the vortex intensity at a point but also an indicator of the direction of

flow rotation (clockwise or anti-clockwise). In this figure the YZ plane is shown at (a) $X/D=-1$ , (b) $X/D=0$ , (c) $X/D=1$ , (d) $X/D=3$ . From figure (a) one can see the beginning of the CRVP in the auxiliary holes. From figure (b) the nascent stages of the single hole configuration and the main hole of the auxiliary hole configuration are seen. Notable differences in the intensity and form of the CRVP structure is seen. The auxiliary hole CRVPs position themselves over the CRVP of the main hole, with the sides have opposite signs of helicity. The effect of this is seen in figure (c) (Figure zoomed on purpose to show the features better) where the auxiliary hole configuration presents an overall reduced helicity intensity

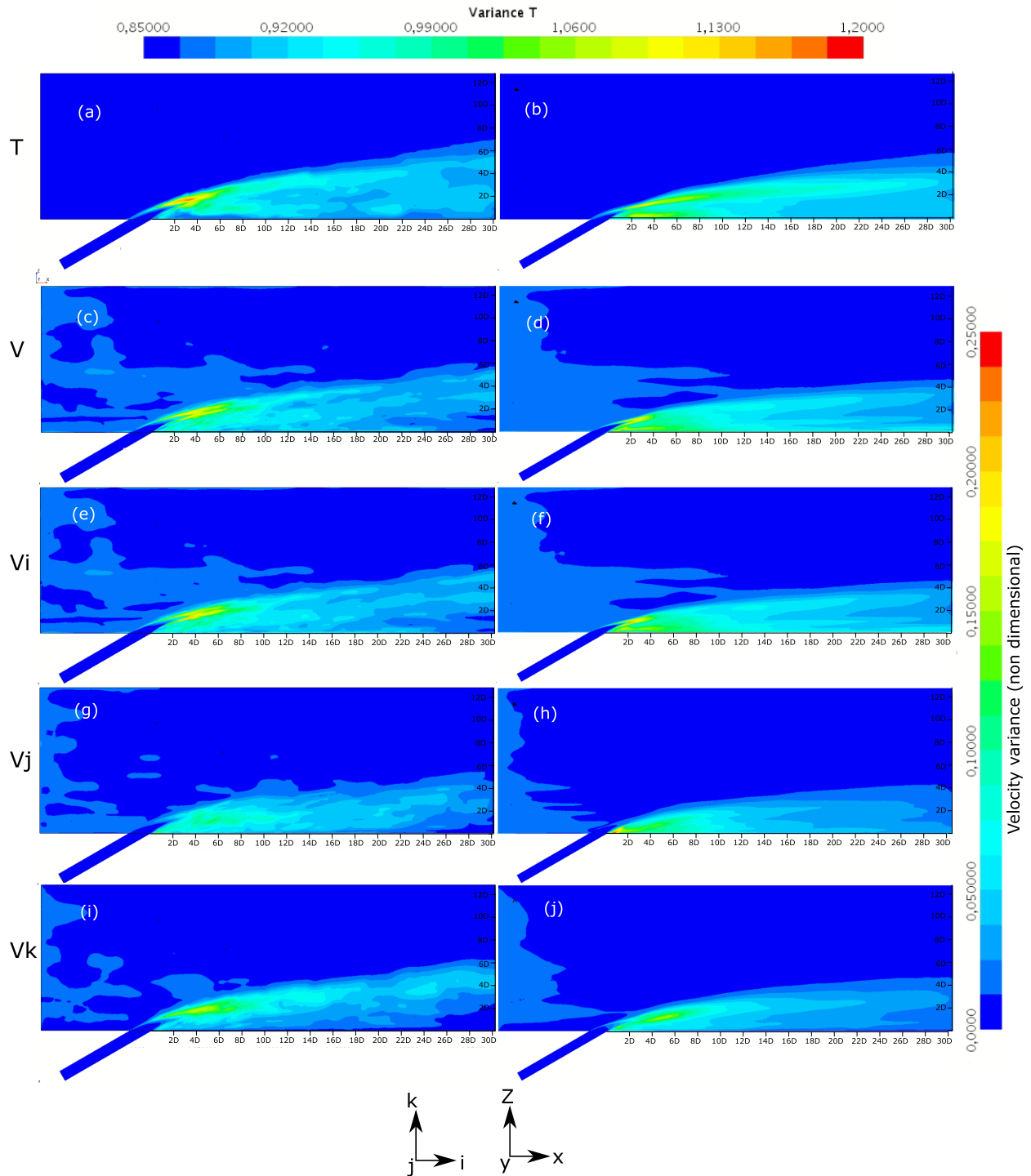


Fig. 15. Variance contours for the single hole configuration and auxiliary hole configuration in the central plane. (a) and (b) present the variance in temperature; (c) and (d) present the variance in velocity magnitude; (e) and (f) present the variance in the  $i$  component of velocity; (g) and (h) present the variance in the  $j$  component of velocity; (i) and (j) present the variance in the  $k$  component of velocity.

while remaining close to the wall. This is due to the auxiliary hole jets staying above the main hole jet which prevents the upward movement of the jet. This feature is not present in the single hole case and hence the CRVP promotes the upward movement of the jet, all the while dragging the main flow into the jet stream. Further downstream at  $X/D=3$ , the over all intensity of the CRVP vortex is reduced, but the single hole

case continues to rise upwards. In the case of the auxiliary hole configuration, the rate of increase in the height of the flow remains lower as compared to the single hole case. For example, in Figure (c), the single hole case CRVP is higher by  $0.5D$  in height along  $Z$  direction as compared to auxiliary hole case.

This explanation is supported by an instantaneous veloc-

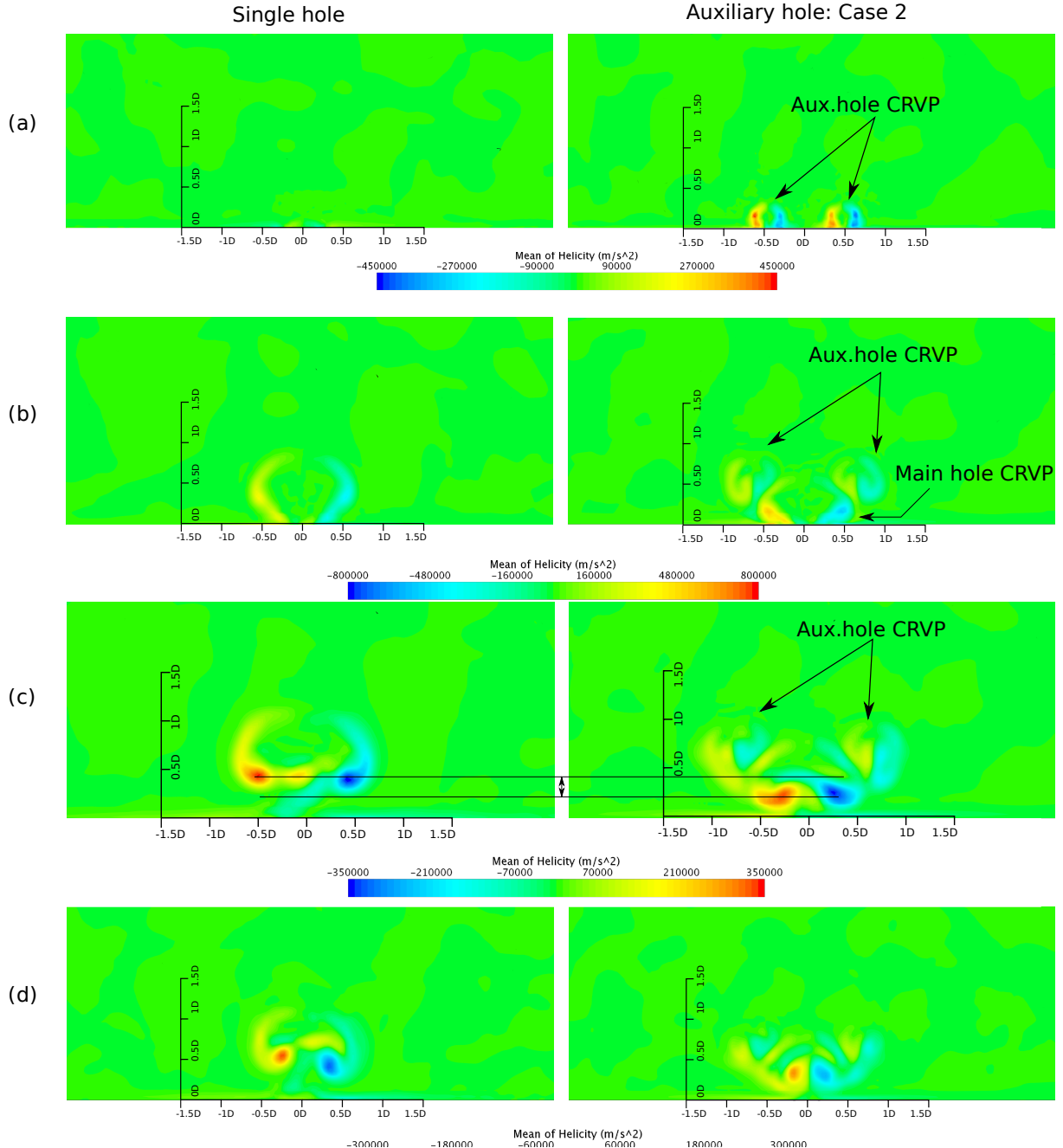


Fig. 16. Front view of the mean helicity contours for the single hole and the auxiliary hole configuration at various planes (a)  $X/D=-1$ , (b)  $X/D=0$ , (c)  $X/D=1$ , (d)  $X/D=3$ .

ity and vorticity field vector visualisation in figure 17 showing the YZ plane at  $X/D=3$ . The figure (a) shows the velocity vector field of the single hole case and (b) shows the corresponding vortex vector field. The direction of the rotation of the flow is markedly seen from the two figures and the CRVP can be identified. The CRVP of the auxiliary hole system represented in (c) and (d) is a more complex. The main hole CRVP shows an opposite direction to the rotation of the auxiliary holes. The effect is a reduced vortex intensity in the entire system (figure (d)) as compared to the single hole system (figure (b)). To further reinforce this point, the instantaneous iso-contours of the Q-criterion are presented.

It is defined as

$$Q = (||\Omega||^2 - ||S||^2) \quad (3)$$

where  $\Omega$  is known as the rotation rate or vorticity tensor and  $S$  is the strain rate. Positive values of  $Q$  represent presence of pure rotation.

Constant values of  $Q=Uc^2/D^2$  colored with mean helicity values to identify the direction of rotation are shown in the figures 18 and 19. In figure 18, a top view of the iso-contours of the Q-criterion are presented. The single hole

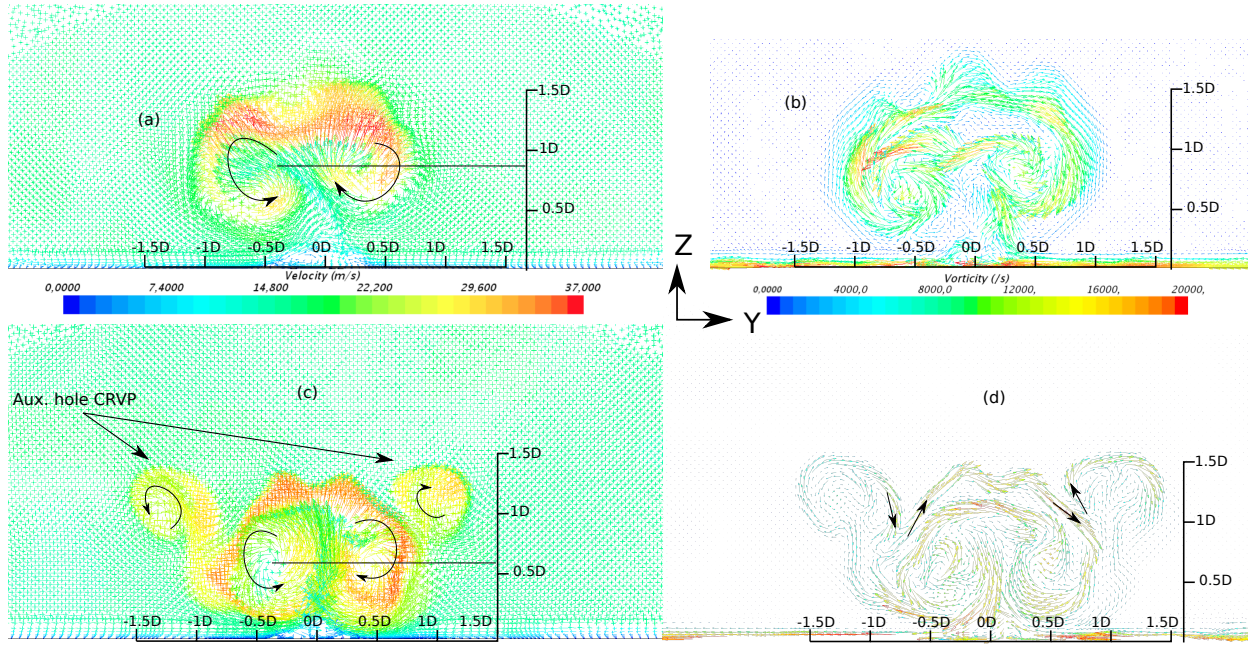


Fig. 17. Instantaneous velocity (a, c) and vorticity (b,d) contours for the single hole and auxiliary hole configuration at  $X/D=3$  plane. Figures (a) and (b) represent the single hole case, while (c) and (d) represent the auxiliary hole configuration.

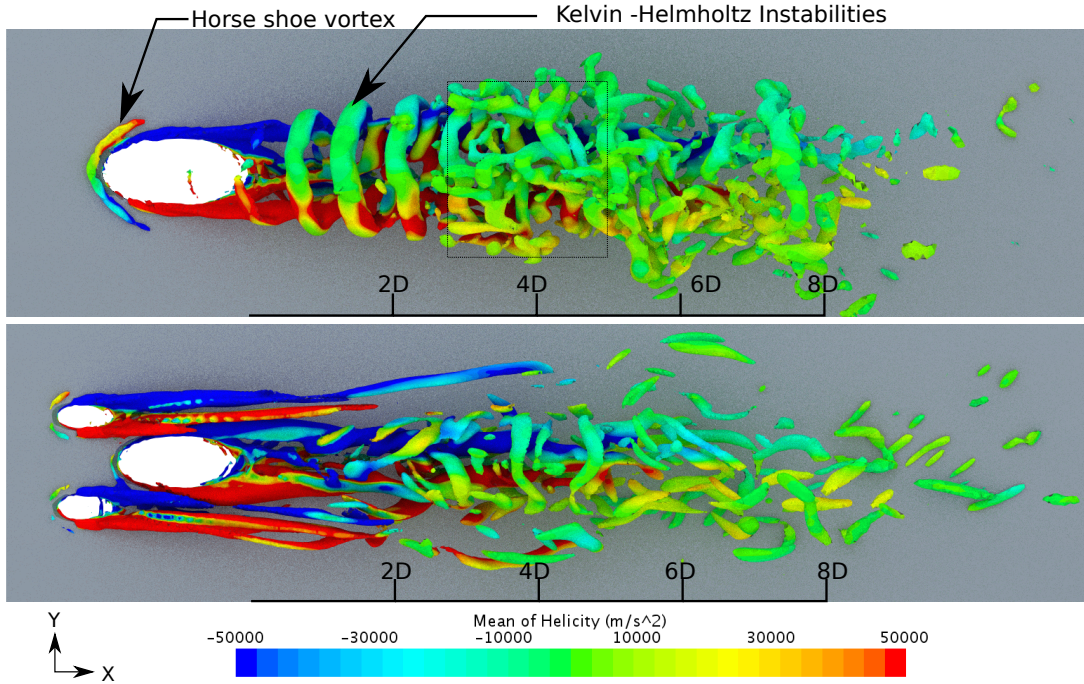


Fig. 18. Top view of the iso-contours of Q-criterion colored with helicity values. Note: the color bar is limited to -50000 and 50000 to better highlight the vorticity features of the film cooling configurations.

case clearly highlights various coherent structures like the development of the horseshoe vortex upstream of the hole, jet-shear layer vortices and the CRVP formation at the edges of the hole exit. The prominent negative and positive arms of the CRVP eventually mix at downstream locations at  $X/D > 2$  and it is difficult to identify coherent structures. After this point, the mixing is three dimensional and there is no preferred direction. The figure in the bottom, the auxiliary hole

configuration shows the development of horse shoe vortices upstream of each of the three holes. The formation of the jet-shear layer vortex system for the main hole is seen further downstream. The most notable feature is the positioning and the interaction of the CRVPs arising from the auxiliary holes and the main hole. The negative arm of the main hole is positioned near the positive arm of the left auxiliary hole and the positive arm of the main hole CRVP is positioned near the

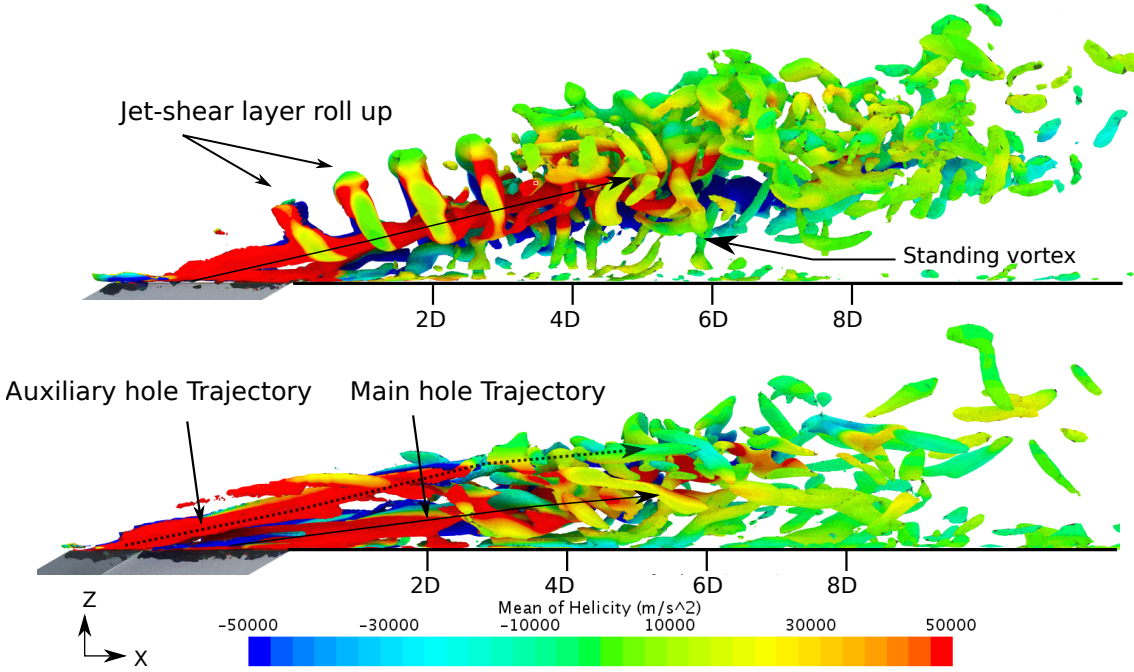


Fig. 19. Side view of the iso-contours of Q-criterion colored with helicity values. Note: the color bar is limited to -50000 and 50000 to better highlight the vorticity features of the film cooling configurations.

negative arm of the right auxiliary hole CRVP. This as explained in the earlier sections, helps in reducing the strength of the overall CRVP of the auxiliary hole system as compared to the single hole system.

Figure 19 further adds clarity to the explanation of why the CRVP height and intensity of the auxiliary hole system is lower. The jet ejecting from the single hole case directly meets the freestream and almost immediately the mixing process happens through the formation of the jet-shear layer vortices. Additionally, there are no barriers to prevent the jet from rising higher in Z direction nor protection in the lateral sides. However in the case of the auxiliary hole arrangement, the jets with high velocity ejecting from the auxiliary holes are the first to be in contact with the main flow and experience a force pushing them towards the main flow direction. Just downstream of these holes, the main hole jet is ejected outwards but due to the protection from the auxiliary hole jets in the lateral directions which also provide a slight downward force helping the main hole jet to stay closer to the wall. The downward force is due to the pulling action of the opposite pairing of the arms of the CRVP in the main hole and auxiliary hole in addition to the downward pushing imparted by the main flow on the auxiliary hole jets.

## 5 Conclusion and inferences

The entire explanation is summarised in the figure 20 which is a schematic representation of the single hole and auxiliary hole CRVP formation and evolution. The entire process can be summarised as

1. The major contribution to the CRVP intensity is the

shear experienced by the ejected jet on its sides, which decide the direction of the CRVP rotation.

2. The initial vortex is aligned in a plane horizontal to the wall supporting the hole ( $Z/D < 0.5$ ). At later stages, the bending of the jet due to the momentum of the main flow causes the CRVP structure to bend along also.
3. At locations that are downstream ( $X/D > 3$ ) from the hole, it can be noticed that the CRVP is completely perpendicular to the wall.
4. This perpendicularity promotes the ingestion of the hot main flow into the cold jet axis, effectively reducing the effectiveness of the cold injected jet near the wall. This means more mixing which is detrimental to the film cooling process.
5. The auxiliary hole configuration is designed to reduce the height and intensity of the CRVP. The idea is to protect as much as possible the sides of the main hole from the shearing due to the interaction of the jet and the main flow.
6. The relative velocity is drastically reduced due to the presence of the auxiliary hole jets and hence the shear force is also reduced. Additionally, the negative-positive arm interaction of the CRVPs in the main hole and auxiliary hole jets contribute to the reduction in the CRVP intensity of the main hole.

## 6 Acknowledgements

This work was partially funded by the French Government program “Investissements d’Avenir” (EQUIPEX GAP, reference ANR-11-EQPX-0018). The authors gratefully ac-

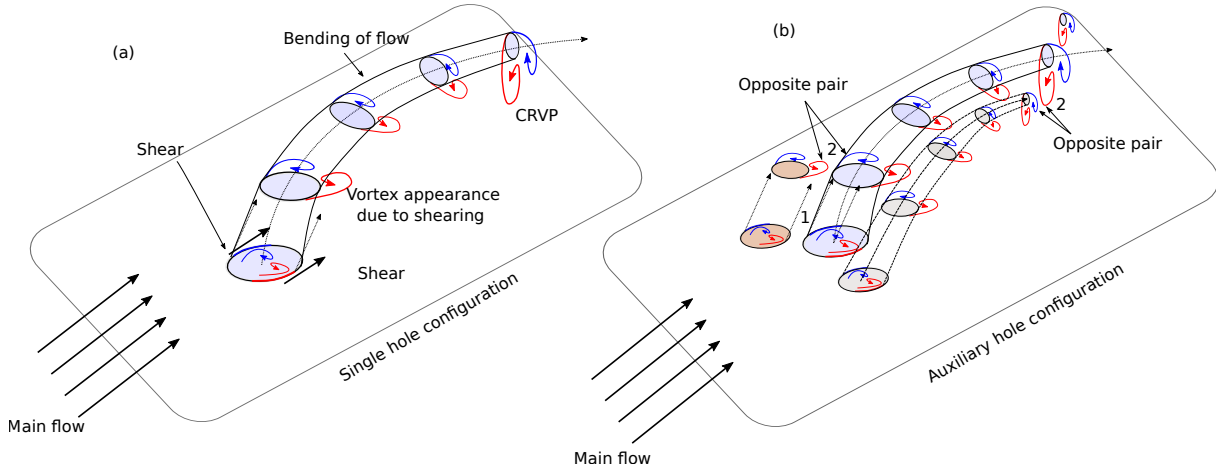


Fig. 20. Illustration of the working mechanism in the single hole and auxiliary hole configurations.

knowledge the scientific help of Dr.Lorenzo Mazzei from ERGON research in this work.

performance". pp. 1187–1196.

## References

- [1] Fric, T., and Roshko, A., 1994. "Vortical structure in the wake of a transverse jet". *Journal of Fluid Mechanics*, **1994**, pp. 1–47.
- [2] Walters, D. K., and Leyklek, J. H., 2000. "A detailed analysis of film-cooling physics: part i—streamwise injection with cylindrical holes". *J. Turbomach.*, **122**(1), pp. 102–112.
- [3] Andreopoulos, J., and Rodi, W., 1984. "Experimental investigation of jets in a crossflow". *Journal of Fluid Mechanics*, **138**, pp. 93–127.
- [4] Mahesh, K., 2013. "The interaction of jets with cross-flow". *Annual review of fluid mechanics*, **45**, pp. 379–407.
- [5] Kelso, R. M., Lim, T., and Perry, A., 1996. "An experimental study of round jets in cross-flow". *Journal of fluid mechanics*, **306**, pp. 111–144.
- [6] Keffer, J., and Baines, W., 1963. "The round turbulent jet in a cross-wind". *Journal of Fluid Mechanics*, **15**(4), pp. 481–496.
- [7] Haven, B. A., and Kurosaka, M., 1997. "Kidney and anti-kidney vortices in crossflow jets". *Journal of Fluid Mechanics*, **352**, pp. 27–64.
- [8] Baek, S. I., and Ahn, J., 2021. "Large eddy simulation of film cooling involving compound angle holes: Comparative study of les and rans". *Processes*, **9**(2), p. 198.
- [9] Addad, Y., Gaitonde, U., Laurence, D., and Rolfo, S., 2008. "Optimal unstructured meshing for large eddy simulations". In *Quality and reliability of large-eddy simulations*. Springer, pp. 93–103.
- [10] Nicoud, F., and Ducros, F., 1999. "Subgrid-scale stress modelling based on the square of the velocity gradient tensor". *Flow, turbulence and Combustion*, **62**(3), pp. 183–200.
- [11] Harrison, K. L., and Bogard, D. G., 2008. "Comparison of rans turbulence models for prediction of film cooling